Hydration fronts in packed particle beds of salt hydrates

Journal of Energy Storage 71 (2023) 108158

Contents lists available at ScienceDirect

Journal of Energy Storage

journal homepage: www.elsevier.com/locate/est

Research papers

Hydration fronts in packed particle beds of salt hydrates: Implications for heat storage

Henk Huinink [a,b,*], Stan de Jong [b], Vera Houben [b]

[a] Eindhoven Institute of Renewable Energy Systems, Eindhoven University of Technology, PO Box 513, Eindhoven 5600 MB, the Netherlands
[b] Transport in Permeable Media group, Department of Applied Physics, Eindhoven University of Technology, PO Box 513, Eindhoven 5600 MB, the Netherlands

ARTICLE INFO

Keywords:
Thermochemical energy storage
Salt hydrates
Hydration
Mathematical model
Hydration front

ABSTRACT

Hydration of packed beds of salt hydrate particles underpins the working principle of low temperature thermochemical energy storage (TCES). Typically, the salt hydrate particles are millimeter sized. An isothermal model for packed bed hydration is formulated, and it is shown that for millimeter sized particles hydration can be described as an advection-reaction process. Traveling wave solutions have been obtained that describe a moving hydration front. The speed of the hydration front is about five orders of magnitude slower than the air velocity in the particle bed. The width of the hydration front is under relevant TCES conditions between 10 and 100 cm. Therefore, hydration fronts will only develop in meter-sized packed beds. A constant hydration rate (and power output) is related to the existence of a traveling hydration front. Therefore, constant hydration rates and power output can only be expected for meter sized TCES reactors. Finally, the influence of temperature gradients is analyzed for the case that the front width is smaller than the bed size. The temperature lift and power output are calculated. Future steps should involve a more detailed description of temperature gradients and a quantitative analysis of finite size effects.

1. Introduction

Salt hydrates are salts with water incorporated in the crystal lattice. The uptake of water by a salt is called hydration and the reverse process dehydration. These reactions can be described with the following reaction equilibrium.

$$Salt{\cdot}\alpha H_2O\ (s) + (\beta - \alpha)H_2O\ (g) \rightleftharpoons Salt{\cdot}\beta H_2O\ (s) \quad (1)$$

Here *Salt* refers to a unit of salt: *Salt* = K_2CO_3, $MgCl_2$, Na_2S, … The parameters α and β indicate the moles of water molecules per mole of unit salts. Depending on the water vapor pressure p [Pa] and temperature T [K] a salt either hydrates or dehydrates.

For decades salt hydration has been studied in view of its role in salt weathering [1–3]. The hydration reaction involves uptake of water molecules leading to expansion of the material. When salt crystals are trapped in the pore system of a rock and start to hydrate, the crystals exert force on the rock matrix that can lead to crack formations [4,5]. In the last decade salt hydrates have gained attention also from the area of renewable energy in view thermal energy storage [6–10]. The hope is that the principle of salt hydration can be used to store energy. For every mole of water binding to a salt (hydration) a fixed amount of energy is released in the form of heat. This amount of energy must be supplied to drive the opposite reaction (dehydration). The reversibility of the reaction makes the principle suitable for thermochemical energy storage (TCES). In general, TCES technology uses a reversible reaction between a solid or liquid with a gas for storing thermal energy [11,12].

The core of a salt hydrate TCES-device is a packed bed of salt particles. The salt particles are manufactured from salt powder, are typically millimeter sized and contain porosity [13–16]. As water vapor needs to have good access to the salt hydrate particles, the permeability of the bed is crucial to facilitate the flow of water vapor through the bed. In general, there exists two ways to drive the water flux relating to two types of systems, referred to as open and closed systems [17,18]. The first class of systems, often called closed systems, operate under pure water vapor condition [19–21]. Under these conditions water vapor diffusion is extremely fast and sufficient to have good reaction rates, but heat transfer is limiting the power output. A second class of systems operates under atmospheric conditions: i.e., besides water vapor there is air as carrier gas. These systems are often called open systems [22,23], but there are variants under investigation that work with a closed loop [24]. Under these conditions water vapor diffusion is slow and forced

* Corresponding author at: Eindhoven Institute of Renewable Energy Systems, Eindhoven University of Technology, PO Box 513, Eindhoven 5600 MB, the Netherlands.
E-mail address: h.p.huinink@tue.nl (H. Huinink).

https://doi.org/10.1016/j.est.2023.108158
Received 23 December 2022; Received in revised form 24 May 2023; Accepted 19 June 2023
Available online 29 June 2023

Nomenclature

A_p	particle surface area, m^2
$c(z,t)$	local water vapor concentration, mol/m^3
c_0	water vapor concentration at the entrance of the bed, mol/m^3
c_{eq}	equilibrium water vapor concentration, mol/m^3
c_{ex}	water vapor concentration at the exit of the bed, mol/m^3
Δc	water vapor concentration difference over the bed, mol/m^3
C_{air}	molar heat capacity of air, J/mol K
C_n	constant related to a particular diffusion limited reaction model
D_{air}	water vapor diffusivity in air, m^2/s
D_b	water vapor dispersion coefficient in the bed, m^2/s
$D_{b,0}$	water vapor diffusion coefficient in the bed, m^2/s
D_p	water vapor diffusivity inside a porous particle, m^2/s
Da_b	Damköhler number for the particle bed
Da_p	Damköhler number for the salt hydrate particle
$f(t)$	position of the hydration front, m
$F(X)$	reaction pathway
H	standard enthalpy of dehydration, J/mol
k	kinetic coefficient, m^3/mol s
L	bed length, m
n	type of diffusion limited reaction
p	water vapor pressure, Pa
p^0	standard pressure (1 atm), Pa
P	power per area, W/m^2
Pe	Peclet number
q	volume flux of the air, m/s
r	particle size, m
R	gas constant, 8.314 J/mol K
S	standard entropy of dehydration, J/mol K
t	time, s
Δt_{CRP}	duration of the constant rate period, s
$\Delta t_{CRP,I}$	duration of phase I of the constant rate period, s
$\Delta t_{CRP,II}$	duration of phase II of the constant rate period, s
Δt_{FRP}	duration of the falling rate period, s
Δt_{RRP}	duration of the rising rate period, s
T	temperature, K
T^*	temperature at which the hydration reaction stops, K
T_{in}	input temperature, K
T_{out}	output temperature, K
ΔT	temperature lift over the particle bed, K
U	average air velocity in the bed, m/s
V	velocity of the hydration front, m/s
V_p	particle volume, m^3
W	front width, m
$X(z,t)$	local conversion
X^*	threshold value of the conversion
z	position, m
α	moles of water per moles of salt units of the lower hydrate
β	moles of water per moles of salt units of the higher hydrate
γ	volumetric reaction density, mol/m^3
η	moving coordinate, m
$\widehat{\eta}$	dimensionless moving coordinate
ξ_D	characteristic dispersion length scale, m
ξ_R	characteristic reaction length scale, m
$\xi_{R,D}$	characteristic reaction length scale for diffusion limited reactions, m
$\xi_{R,\kappa}$	characteristic reaction length scale for constant rate reactions, m
ρ	molar density of salt in a salt hydrate particle, mol/m^3
ρ_{air}	molar density of air, mol/m^3
ρ_α	crystal density of the α-phase, mol/m^3
ρ_β	crystal density of the β-phase, mol/m^3
$\Delta\rho_w(z,t)$	the local amount of absorbed water per volume, mol/m^3
$\Delta\rho_{w,max}$	the maximal amount of absorbed water per volume, mol/m^3
σ	global reaction rate, mol/m^2s
τ	tortuosity
ϕ_b	porosity of the particle bed
ϕ_p	porosity of a salt hydrate particle
$\psi(z,t)$	dimensionless vapor concentration

advection is used to drive the water vapor into the particle bed. In this paper we model this class of systems, where water vapor is brought to the salt by advection.

There have been many attempts to model the hydration of salt particles in TCES devices [18,25,26,27,28,29,30,31]. These studies are numerically in nature and aim to predict the performance of a certain device or configuration (power output and temperature lift). These studies have put a lot of effort in solving simultaneously the partial differential equations (PDE) for the water vapor phase, the solids, and the energy. Due to the numerical approach and the specificity of the adopted device configurations these studies generate limited insights in the salt hydration process as such. On fundamental level several fundamental questions remain unanswered. First, under what conditions do hydration fronts develop in a packed bed? Second, how fast do such fronts travel? Third, what is the shape of such a hydration front? Underneath all these questions is the central question: how does the hydration rate on the bed scale relate to the hydration kinetics of a single salt hydrate particle? Concise analytical solutions as answers to these questions would be of great help for designers of TCES devices.

The mathematics behind salt hydration obeys the so-called class of advection-diffusion-reaction (ADR) equations. Analytical solutions seem to be available for a single PDE given that it is a linear equation or has a very specific non-linear form. To describe salt hydration, the problem of interest, at least a set of two or three coupled PDE's must be solved. The reaction term that couples these PDE's can be described with analytical models that have been validated by experiments. Unfortunately, the mathematical nature of the reaction term introduces non-linearity into the problem. To the best of authors knowledge there have been no attempts to come up with analytical or quasi-analytical solutions for the problem of salt hydration.

This study aims to study hydration fronts in packed beds of salt hydrate particles in relation to the hydration kinetics of individual particles. Although the analysis is rather general, special attention will be paid to millimeter sized salt hydrate particles relevant for TCES applications. To simplify the problem, we mainly focus on isothermal conditions. We discuss traveling wave solutions for obtaining the velocity, width, and shape of a hydration front. The relation between front shape and the salt particle reaction kinetics will be investigated with a focus on diffusion limited reaction kinetics inside the particles. Properties of several salts ($CuCl_2$, K_2CO_3, LiCl, $MgCl_2$, $SrBr_2$ and $SrCl_2$) will be used to parameterize the model and assess certain model assumptions. Note that these salts are representative for many salt hydrates and are widely studied in view of TCES applications [6–9]. Quantitative predictions of the speed and width of hydration fronts will be done based on existing experimental data. Furthermore, the implications for finite sized TCES reactors will be discussed. Finally, we assess the influence of temperature gradients on properties like the hydration front velocity and variables characterizing TCES performance (temperature lift and power output).

2. Basic model

We consider a homogenous packed bed of millimeter sized salt particles with a porosity ϕ_b [−] at a fixed temperature T [K]. Salt particles are made from compressed salt powder and have porosity ϕ_p [−] and tortuosity τ [−]. A schematic picture of the packed bed is shown in Fig. 1. Air flows through the bed with a volume flux q [m/s], which is often called superficial velocity. The air carries water vapor with a density $c(z,t)$ [mol/m^3] that varies with time t [s] and position z [m]. At the entrance and exit of the bed the water vapor has densities c_0 [mol/m^3] and c_{ex} [mol/m^3], respectively. The water vapor reacts with the salt particles resulting in an increase of the hydration state of the salt. In this paper we limit ourselves to single step hydration reactions. The degree of hydration is quantified with a so-called conversion parameter $X(z,t)$ that can vary between 0 and 1: $X(z,0) = 0$ and $X(z,\infty) = 1$.

$$X(z,t) \equiv \Delta\rho_w(z,t)/\Delta\rho_{w,max} \tag{2}$$

In this definition $\Delta\rho_w(z,t)$ [mol/m^3] is the amount of water absorbed per volume, and $\Delta\rho_{w,max}$ [mol/m^3] is the maximal amount that can be absorbed. It is assumed that the salt particles neither change size or shape during hydration. In case X strongly varies between the entrance and the exit, a hydration front exists that has a position $f(t)$ [m].

As the gas behaves ideal, c can be linked with the water vapor pressure via the ideal gas law: $p = cRT$. Hydration or dehydration occurs when $c(z,t) > c_{eq}$ or $c(z,t) < c_{eq}$, respectively. Here c_{eq} [mol/m^3] is the equilibrium vapor concentration that is given by the Clausius-Clapeyron equation:

$$c_{eq} = \frac{p^o}{RT} exp(S/R) exp(-H/RT) \tag{3}$$

Here H [J/mol] and S [J/mol K] are the standard enthalpy and entropy of dehydration per mole water ($H > 0$ and $S > 0$). Further, $R = 8.314$ J/mol K is the gas constant and p^o [Pa] the standard pressure (1 atm). In this paper we only consider hydration: $c(z,t) > c_{eq}$.

By working with a single spatial coordinate z we already reduced the problem to 1D. This has several implications. First, the particle packing, and the air flow is assumed constant all over the bed. Second, each particle at position z experiences the same water vapor concentration at its surface and therefore has the same reaction kinetics driven by the difference $c - c_{eq}$.

Salt hydration belongs to the category of solid-gas reactions and is often described with the general kinetic equation (GKE) [32–34]. A detailed discussion of the GKE-approach is beyond the scope of this paper. Here we adopt a specific form that has recently been validated for salt hydrate particles [16].

$$\frac{\partial X}{\partial t} = kF(X)\theta(1-X)(c - c_{eq}) \tag{4}$$

In this equation k [m^3/mol s] is a kinetic coefficient reflecting the nature of the hydration reaction. In case of a diffusion limited reactions, it is directly connected with the water vapor diffusion coefficient in the salt particle D_p [m^2/s].

$$D_p = \frac{\phi_p}{\tau} D_{air} \tag{5}$$

Here D_{air} [m^2/s] is the diffusivity of water vapor in air. Further, $F(X)$ is a function describing the reaction pathway, respectively. The term $\theta(1-X)(c - c_{eq})$ represents the driving force for the reaction, where $\theta(1-X)$ is a Heaviside step function that guarantees that the reaction stops when all mass has been converted ($X = 1$). In Table 1 an overview is given of the particle reaction models studied in this paper. The expressions for $F(X)$ and k have been obtained from the literature on gas-solid reactions and adapted to the details of salt hydration [35–37]. Several studies on salt hydration have already used this type of modeling [15,16,38].

Four different reaction models for the particles will be explored. First, a constant rate model (CR) that serves as a reference model and is easily solvable. Secondly, we will investigate three diffusion limited reaction models (DLR_n and $n = 1,2,3$) related to three geometries (plates, cylinders, and spheres). The parameter n is a shape factor quantifying the particle surface area A_p [m^2] per volume of the particle V_p [m^3] given a particular particle size r [m].

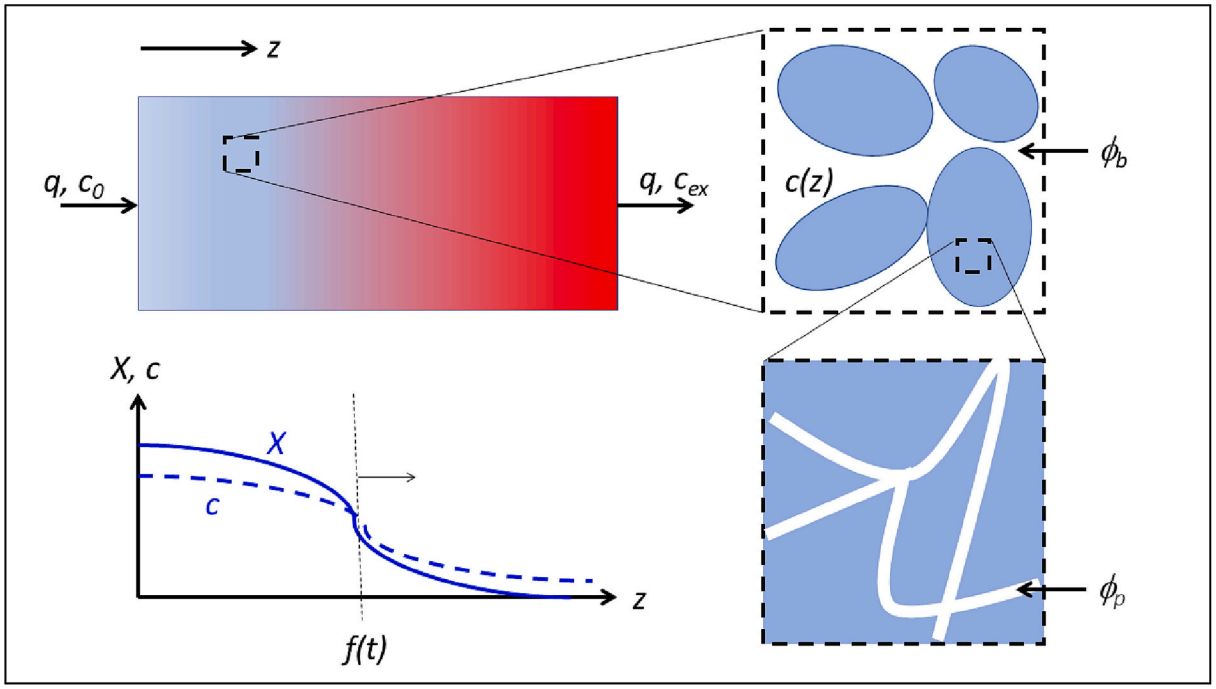

Fig. 1. Schematic picture of the modeling approach of hydration of a salt bed. A 1D homogenized model will be used, where flow and porosity are assumed to be homogeneous (upper left). The time evolution of the water vapor concentration c and conversion X (the degree of salt hydration) will be calculated (lower left). The reaction term in the equations will account for the particle shape (upper right) and its internal structure (lower right).

Table 1
Overview of the investigated reaction models. The CR (constant rate) model assumes that the hydration kinetics of the particle is not limited by water vapor transport into the particle and is constant. The three DLR (diffusion limited rate) models assume that the hydration rate is limited by water vapor diffusion into the particle. Three particle shapes are investigated: plates ($n = 1$), cylinders ($n = 2$) and spheres ($n = 3$).

Model	$F(X)$	k
CR		
Constant rate	1	κ
DLR_1		
Diffusion limited reaction of infinite flat plates	$\frac{1}{X}$	$\frac{D_p}{r^2(\beta-\alpha)\rho}$
DLR_2		
Diffusion limited reaction of infinite cylinders	$\frac{-4}{ln(1-X)}$	$\frac{D_p}{r^2(\beta-\alpha)\rho}$
DLR_3		
Diffusion limited reaction of spheres	$\frac{3}{(1-X)^{-1/3}-1}$	$\frac{D_p}{r^2(\beta-\alpha)\rho}$

$$n \equiv \frac{A_p r}{V_p} \tag{6}$$

These models have been validated for millimeter sized porous K_2CO_3 particles [16], allowing us to do quantitative predictions for hydration fronts under relevant TCES conditions. It must be stressed that the DLR models overestimate the reaction kinetics at the start of the process, $\lim_{X\to 0} F(X) = \infty$, where the intrinsic reaction rate of the salt limits the speed of hydration. Therefore, $F(X)$ will be constrained to a finite value at for small values of X.

In Table 1 r [m] is the particle radius case of cylindrical and spherical particles, and half the particle thickness in case of plate-like particles. Further, ρ [mol/m^3] is the molar density of salt in the salt particle, which is of course related to the crystal density of the starting phase ρ_α [mol/m^3] and the particle porosity: $\rho = \rho_\alpha\left(1-\phi_p\right)$.

The water vapor concentration inside the packed bed varies in time and space due to advection, diffusion, and reaction. This can be described with the following ADR equation.

$$\phi_b \frac{\partial c}{\partial t} = \phi_b D_b \frac{\partial^2 c}{\partial z^2} - \phi_b U \frac{\partial c}{\partial z} - \gamma k \theta (1-X) F(X)\left(c - c_{eq}\right) \tag{7}$$

Here U [m/s], D_b [m^2/s] and γ [mol/m^3] are the air velocity, dispersion coefficient and the volumetric reaction density, respectively. Note that there is a direct relation between the volume flux and the air velocity: $q = U\phi_b$. The parameter γ describes the required amount of water to convert all salt in a certain volume.

$$\gamma = (1-\phi_b)(\beta-\alpha)\rho = (1-\phi_b)\left(1-\phi_p\right)(\beta-\alpha)\rho_\alpha \tag{8}$$

The dispersion coefficient D_b reduces to the water vapor diffusivity at low air velocities.

From now on, we will work with an infinite packed bed. In such a bed the boundary conditions for the conversion are well defined: $X(-\infty, t) = 1$ and $X(+\infty, t) = 0$. Furthermore, we choose $c(-\infty, t) = c_0$ and $c(+\infty, t) = c_{eq}$. As the temperature is fixed the vapor density drop over the bed has a fixed value: $\Delta c \equiv c_0 - c_{eq}$ [mol/m^3].

3. Traveling waves

3.1. Front velocity

In an infinite system a hydration front always develops as its width cannot exceed the boundaries of the system. Since the vapor consumption rate is constant, $q\Delta c$, one might expect that the hydration front also travels with a constant velocity V [m/s]. It must be remarked that ADR equations often have traveling wave solutions [39–41]. This front velocity V can be found via the following mass conservation equation.

$$\gamma V = \phi_b (U - V)\Delta c \tag{9}$$

The left-hand side of the equation describes the amount of water reacting with the salt in the front area. The right-hand side of the equation describes the difference between the water vapor fluxes upstream and downstream the front. By rewriting this equation, one finds an equation for the front velocity.

$$V = U \frac{\phi_b \Delta c/\gamma}{1 + \phi_b \Delta c/\gamma} \tag{10}$$

The factor $\phi_b\Delta c/\gamma$ represents the ratio between the amount of water in the air phase that can react, $\phi_b\Delta c$, and that has reacted with the salt, γ. With the help of Eq. (8) it can be shown that this ratio equals

$$\frac{\phi_b \Delta c}{\gamma} = \frac{\phi_b}{(1-\phi_b)\left(1-\phi_p\right)} \frac{\Delta c}{(\beta-\alpha)\rho_\alpha} \tag{11}$$

It follows from these equations that the velocity of the hydration front is fully decoupled from the hydration kinetics of the individual particles. Note that factor $\phi_b\Delta c/\gamma$ is dominated by the ratio $\Delta c/(\beta-\alpha)\rho_\alpha$ as the vapor density c is much lower than the density of the absorbed water in the crystalline phase $(\beta-\alpha)\rho_\alpha$. Therefore, in most cases $\phi_b\Delta c/\gamma \ll 1$ and

$$V \approx U\phi_b \Delta c/\gamma \tag{12}$$

The main conclusion here is that the velocity of the hydration front will always be orders of magnitude slower than the air velocity. The vapor phases contain much less water than is absorbed by the salt.

To explore the existence of traveling wave solutions, a moving spatial coordinate η [m] is adopted in which the position of the front has a fixed value.

$$\eta \equiv z - Vt \tag{13}$$

Furthermore, we simplify the equations by working with a dimensionless vapor concentration field ψ that like X varies between 0 and 1.

$$\psi \equiv \frac{c - c_{eq}}{c_0 - c_{eq}} \tag{14}$$

With Eq. (13) and Eq. (14) one can rewrite the Eq. (4) and Eq. (7) to

$$V\frac{dX}{d\eta} + k\theta(1-X)F(X)\Delta c\psi = 0 \tag{15}$$

and

$$\phi_b D_b \frac{d^2\psi}{d\eta^2} - \phi_b (U-V)\frac{d\psi}{d\eta} - \gamma k\theta(1-X)F(X)\psi = 0 \tag{16}$$

This set of equations has the boundary conditions $X(-\infty, t) = 1$, $X(+\infty, t) = 0$, $\psi(-\infty, t) = 1$ and $\psi(+\infty, t) = 0$.

Note that the set of PDE's have been transferred into a set of ODE's (ordinary differential equations). Before solving this set of equations, the role of dispersion/diffusion will be discussed in more detail.

3.2. The role of dispersion or diffusion

To judge the roles of dispersion and diffusion as modes of transport, Eq. (16) will now be analyzed in more detail. First a length scale ξ_R [m] is defined that characterizes the reaction.

$$\xi_R \equiv \frac{\phi_b (U-V)}{\gamma k} \tag{17}$$

In case of the CR model, we will refer to this length scale with $\xi_{R,\kappa}$. In case of diffusion limited reaction kinetics (DLR models), one can obtain the following equation by using the equations for k as listed in Table 1:

$$\xi_{R,D} \equiv \left(\frac{\phi_b}{1-\phi_b}\right)\frac{r^2(U-V)}{D_p} \tag{18}$$

An interesting feature of this expression for ξ_R is that it neither depends on the water vapor pressure gradient Δc driving hydration nor on the water vapor density in the salt hydrate. The only particle properties that matter are its size r, and the vapor diffusivity D_p. In case $U \gg V$ Eq. (18) reduces to

$$\xi_{R,D} \approx \left(\frac{\phi_b}{1-\phi_b}\right)\frac{r^2 U}{D_p} \tag{19}$$

With the help of a dimensionless coordinate $\widehat{\eta} \equiv \eta/\xi_R$ Eq. (16) can be rewritten as

$$\frac{\xi_D}{\xi_R}\frac{d^2\psi}{d\widehat{\eta}^2} - \frac{d\psi}{d\widehat{\eta}} - \theta(1-X)F(X)\psi = 0 \tag{20}$$

Here $\xi_D = D_b/(U-V)$ is the length scale that shows to what extend dispersion can compete with advection. When $\xi_D/\xi_R \ll 1$, dispersion can be neglected, and advection dominates the vapor transport. It follows from the definition of the length scales that

$$\frac{\xi_D}{\xi_R} = \frac{\gamma k D_b}{\phi_b (U-V)^2} \tag{21}$$

For further quantification of this ratio, again the equations for k of the DLR models are used, see Table 1, in combination with Eq. (8).

$$\frac{\xi_D}{\xi_{R,D}} = \left(\frac{1-\phi_b}{\phi_b}\right)\frac{D_b D_p}{r^2 (U-V)^2} \tag{22}$$

Before being able to judge the importance of vapor dispersion and/or diffusion, first the dispersion constant D_b needs be made more explicit. At low air velocities this constant will converge to the water diffusivity in the bed $D_{b,0}$ [m^2/s]. However, at sufficiently high air velocities random advective motion will increase the value of D_b. To estimate if random advective motions can compete with molecular diffusion, the following Peclet number is analyzed [42].

$$Pe \equiv \frac{Ud}{D_{air}} \approx \frac{2Ur}{D_{air}} \tag{23}$$

In this equation $d = 2r$ is the typical diameter/length scale of the salt hydrate particle. Using typical values $U = 0.1$–1 m/s, $D_{air} = 24$ mm^2/s (20 °C) [43] and $r = 0.3$–3 mm, the estimated Pe varies between 2.5 and 250, which makes that we are in the regime of mechanical dispersion. For our evaluation of the importance of the dispersion for vapor transport, Eq. (16), it suffices to focus on the upper bound for D_b. This upper bound is given by [44]

$$D_b = D_{air}\left(\frac{1}{\tau} + 1.8Pe\right) \approx 3.6\, Ur \tag{24}$$

The last term on the right-hand side of the equation fully ignores the role of molecular diffusion.

With the help of Eq. (24) and using $U \gg V$ it can be shown that

$$\xi_D = \frac{D_b}{U} = 3.6\, r \tag{25}$$

This surprisingly simple relation demonstrates that molecular diffusion or random advective motions (dispersion) only compete with advection on the scale of the particle size itself. By combining Eq. (22) and Eq. (24), and using $U \gg V$, one finds the following equation.

$$\frac{\xi_D}{\xi_{R,D}} \approx 3.6\left(\frac{1-\phi_b}{\phi_b}\right)\frac{D_p}{Ur} \tag{26}$$

For typical values ($D_p = 1$ mm^2/s [16], $\phi_b = 0.5$, $U = 1$ m/s and $r = 1.5$ mm) it can be estimated that $\xi_D/\xi_{R,D} = 2.4{\cdot}10^{-3}$. From this analysis it can safely be concluded that the dispersion/diffusion term of the vapor transport equation can be ignored.

3.3. Purely advective systems

In case dispersion and diffusion can be neglected as transport modes, the differential equation for the vapor phase, Eq. (16), reduces to

$$\phi_b (U-V)\frac{d\psi}{d\eta} + \gamma k \theta (1-X)F(X)\psi = 0 \tag{27}$$

This differential has the same form as the differential for the conversion X. By combination of the differentials for X, Eq. (15), and ψ, Eq. (27), one can show that

$$\phi_b (U-V)\frac{d\psi}{d\eta} = \frac{\gamma}{\Delta c} V \frac{dX}{d\eta} \tag{28}$$

By integrating Eq. (28) with the boundary conditions for X and ψ (both running from 1 to 0) and using Eq. (9), it can be shown that there is a simple linear relation between X and ψ.

$$\psi = X \tag{29}$$

This equation enables us to reduce the set of two ODE's to a single ODE that only depends on either the conversion or the vapor density. Combination of Eq. (27) and Eq. (29) gives:

$$\frac{dX}{d\eta} + \frac{k\gamma}{\phi_b (U-V)}\theta(1-X)F(X)X = 0 \tag{30}$$

This equation demonstrates that in this case there is only one length scale determining the size of the front: ξ_R.

$$\frac{dX}{d\eta} + \xi_R^{-1}\theta(1-X)F(X)\mathrm{X} = 0 \tag{31}$$

With the obtained differential equations for X a full description of the front shape can be obtained. While the detail of the front shape depends on the reaction pathway of the salt hydrate particle $F(X)$, the typical width is more related to length scale ξ_R.

Eq. (31) offers the opportunity to predict front shapes as well from particle reaction models as given in Table 1, which are directly obtained from empirical data via single particle reaction measurement: i.e. TGA measurements on hydration reactions [32,45].

3.4. Front shapes

As we have a closed-form differential equation for the conversion X, Eq. (31), and as we have found that the normalized concentration field ψ is equal to the conversion, Eq. (29), the shape of the hydration front can be obtained. We choose $X(\eta) = 1$ for $\eta \leq 0$. Although other choices would have been possible, this choice simplifies the discussion as solutions must be found $\eta > 0$, where $X < 1$. In case of the CR (constant rate) and DLR$_1$ model (diffusion limited reaction of plate like particles) one can easily find analytical solutions for X as a function of η. In case of the DLR$_2$ (diffusion limited reaction of cylindrical particles) and DLR$_3$ (diffusion limited reaction of spherical particles) models only analytical solutions for the inverse, η as a function of X, can be obtained easily. For reasons of consistency, therefore all solutions will be given in the form $\eta(X)$. The solutions for all for particle models are shown in Fig. 2, and will be discussed in more detail below.

First the CR model is discussed. This model has a simple solution for $\eta(X)$ of the form

$$\eta(X)/\xi_{R,\kappa} = -lnX \tag{32}$$

When $\eta \to \infty$, $X \downarrow 0$. Note that the conversion is an exponential function of the distance, $X(\eta) = exp(-\eta/\xi_{R,\kappa})$, where $\xi_{R,\kappa}$ is the decay length of the function, see Fig. 2.

The DLR$_1$ model has the following solution $0 < \eta/\xi_{R,D} < 1$.

$$\eta(X)/\xi_{R,D} = 1 - X \tag{33}$$

For $\eta/\xi_{R,D} \geq 1$ it holds that $X = 0$. From this equation it follows that

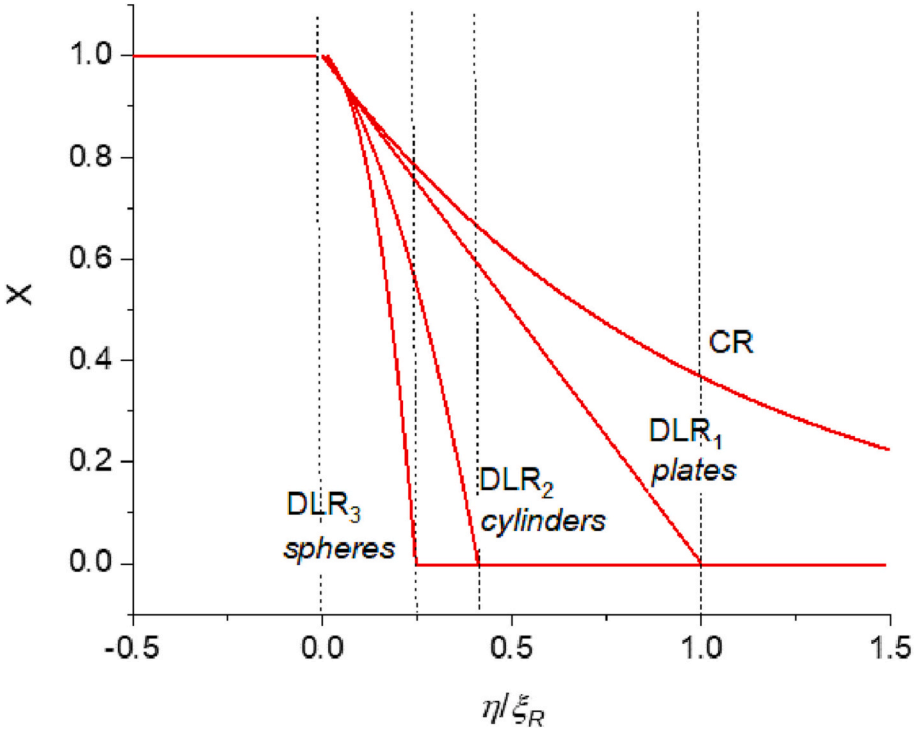

Fig. 2. Front shapes for the different particle reaction models. The positional coordinate η is scaled on the reaction length scale ξ_R. The positional coordinates are chosen such that the point $X = 1$ coincides with $\eta = 0$.

the front linearly decays as a function of distance, $X(\eta) = 1 - \eta/\xi_{R,D}$, for $0 \le \eta/\xi_{R,D} \le 1$.

For $0 < \eta/\xi_{R,D} < \pi^2/24$ the analytical solution of the DLR_2 model equals

$$\eta(X) \Big/ \xi_{R,D} = \frac{1}{4}\left[\pi^2/6 - Li_2(X)\right] \tag{34}$$

Here $Li_2(X)$ is the Polylogarithmic function: $Li_2(X) \equiv \sum_{k=1}^{\infty} k^{-2} X^k$. As $Li_2(1) = \pi^2/6$ and $Li_2(0) = 0$, it can be deduced that the conversion front decays from $X = 1$ to 0 for $\eta/\xi_{R,D} \rightarrow \pi^2/24$.

For $0 < \eta/\xi_{R,D} < \left(ln(3) - \pi/3\sqrt{3}\right)/2$, the DLR_3 model has the following solution

$$\eta(X) \Big/ \xi_{R,D} = \frac{1}{2} ln\left((1-X)^{2/3} + (1-X)^{1/3} + 1\right) - \frac{1}{\sqrt{3}} arctan\left(\frac{2(1-X)^{1/3}+1}{\sqrt{3}}\right) + \frac{\pi}{6\sqrt{3}} \tag{35}$$

From this equation it follows that the conversion front decays from $X = 1$ to 0 for $\eta/\xi_{R,D} \rightarrow \left(ln(3) - \pi/3\sqrt{3}\right)/2$.

A peculiar feature of the DLR models is that the ultimate width of the front zone W [m], the distance over which X decays from 1 to 0, is well defined, see also Fig. 2. The conversion X drops to zero at a well-defined position in space, η, due to the infinite fast reaction rate at $X = 0$, see Table 1. The high reaction rates prevent water vapor to penetrate deeper into the particle bed. A practical implication of this is that W can easily be quantified for the different DLR particle models.

$$W = C_n \xi_{R,D} = C_n \left(\frac{\phi_b}{1-\phi_b}\right) \frac{r^2 (U - V)}{D_p} \tag{36}$$

C_n is a model dependent constant, which values are listed in Table 2. It follows from Eq. (36) that the parameter C_n can be used to compare front widths in particle beds of differently shaped particles with the same internal structure (having the same value of D_p) and the same dimensions (having the same value of r), given that the beds have the same porosity ϕ_b.

Table 2
Predictions for the scaled front width for the particles experiencing diffusion limited hydration kinetics.

Particle model	n	C_n
DLR_1 (plates)	1	1
DLR_2 (cylinders)	2	$\pi^2/24 \approx 0.41$
DLR_3 (spheres)	3	$\left(ln(3) - \pi/3\sqrt{3}\right)/2 \approx 0.25$

The values of C_n demonstrate that a hydration front in bed of plate-like particles can be 4 times wider than in bed of spherical particles with comparable properties.

It follows from Eq. (36) that W increases with U and decreases with an increasing reaction rate, reflected by the parameter D_p. With increasing air velocity, water vapor molecules can travel over longer distances before undergoing a hydration reaction with the salt. Therefore, the zone in which the hydration reaction occurs broadens, and W broadens.

3.5. Modifications of the front shape

An aspect not discussed in Section 3.4, deserving attention, is the validity of the front shapes as predicted by DLR models. As mentioned before, in DLR models the reaction rate goes to infinity at $X = 0$, see Table 1. However, at low conversions no longer vapor diffusion but the intrinsic reaction rate of the salt limits the particle's hydration kinetics. Therefore, DLR models will hold for, $X \ge X^*$, where X^* is a threshold value for the conversion. For $X < X^*$ one should switch to a CR-type of model. A more realistic model combining DLR kinetics for $X \ge X^*$ and CR kinetics for $X < X^*$, might predict front shapes like the DLR models shown in Fig. 2, but with an exponential tail at the leading edge of the front. In this section a composite DLR-CR model will be analyzed, front shapes will be predicted and the value of X^* will be assessed. For

simplicity only the kinetics of plate-like particles will be discussed (the DLR_1 model).

A first order correction to the DLR_1 model would be assuming constant rate phase at low conversion: $X < X^*$. We will refer to this model as the DLR_1-CR model. From the equations listed in Table 1 it follows that

$$kF(X) = \begin{cases} \kappa & \wedge \quad 0 \le X < X^* \\ \dfrac{D_p}{Xr^2(\beta-\alpha)\rho} & \wedge \quad X^* \le X \le 1 \end{cases} \tag{37}$$

As the reaction rate must be continuous at $X = X^*$,

$$X^* = \frac{D_p}{r^2(\beta-\alpha)\rho\kappa} = \frac{1}{Da_p} \tag{38}$$

Here $Da_p = \xi_{R,\kappa}/\xi_{R,D}$ is a type II Damköhler number for the salt hydrate particle that characterizes the tradeoff between transport (diffusion) and reaction limited kinetics [46]. Note that X^* cannot exceed 1 (full conversion). Therefore, diffusion limited reaction kinetics will play a role given that $Da_p \ge 1$.

With the help of Eq. (37) the differential for the front shape, Eq. (30), can be written as

$$\frac{dX}{d\eta} = -\frac{\gamma}{\phi_b(U-V)} \begin{cases} \kappa X & \wedge \quad 0 \le X < X^* \\ \dfrac{D_p}{r^2(\beta-\alpha)\rho} & \wedge \quad X^* \le X \le 1 \end{cases} \tag{39}$$

Note that the continuity of $kF(X)$ at $X = X^* = 1/Da_p$ automatically assure continuity of $dX/d\eta$ at this point. This differential has the following solution

$$X = \begin{cases} 1 - \eta/\xi_{R,D} & \wedge \quad 0 \le \eta < \eta^* \\ Da_p{}^{-1} exp\left(-Da_p[\eta - \eta^*]/\xi_{R,D}\right) & \wedge \quad \eta \ge \eta^* \end{cases} \tag{40}$$

The length scale $\xi_{R,D} = (\phi_b/1-\phi_b)\left(r^2(U-V)/D_p\right)$ is defined by Eq. (18) for $n = 1$.

The location at the front where the reaction kinetics changes from diffusion limited to reaction limited is represented by η^*:

$$\eta^* = \left(\frac{Da_p - 1}{Da_p}\right)\xi_{R,D} \tag{41}$$

As an example, the front shape has been calculated for $Da_p = 5$. The relation between the front shape and the reaction kinetics is shown in Fig. 3. The constant rate period introduces an exponential tail at the leading edge of the hydration front.

4. Reaction regimes for finite sized particle beds

As particle beds in TCES applications are obviously finite sized, the implications of our findings for salt hydration in finite sized systems is briefly discussed in this section. Two issues will be addressed: a) the circumstances needed for development of a hydration front and b) the reaction regimes in case a front develops. In our discussion we will focus on particles with diffusion limited reaction kinetics and use the fact that mostly $U \gg V$. The discussion will be done with the help of the global reaction rate σ [mol/m^{2}s], which is a measure for the power output per area P [W/m^2] of a TCES particle bed: $P = H\sigma$.

$$\sigma(t) = \gamma \frac{d}{dt}\int_0^L X(z,t)dz \tag{42}$$

Here L [m] is the length of the bed. Except during a very small starting phase of duration L/U, the global reaction rate σ can also be quantified by

$$\sigma(t) = \phi_b U(c(0,t) - c(L,t)), \tag{43}$$

given that the difference between the amount of water entering and exiting the system is fully consumed by the hydration reaction. Therefore, Eq. (43) can be used when the water vapor concentration field has reached a quasi-steady state.

The first issue is about the conditions needed for developing a traveling hydration front. This can be assessed on the basis of the ratio of the front width W and the system size L, which is actually a Damköhler number of type I [46].

$$Da_b = \frac{L}{W} \approx \frac{1}{C_n}\left(\frac{1-\phi_b}{\phi_b}\right)\frac{L/U}{r^2/D_p} \tag{44}$$

Note that L/U and r^2/D_p are the advective time scale for the particle bed and the diffusion time scale for a single particle, respectively. Two regimes can be distinguished: $Da_b < 1$ and $Da_b > 1$. When $Da_b < 1$, the particle reaction mainly determines the global response of the bed as X is constant over the bed and

$$\sigma(t) = \gamma L\frac{dX}{dt} = \gamma L\frac{D_p}{r^2(\beta-\alpha)\rho}F(X)\Delta c \tag{45}$$

In case particles obey the diffusion limited reaction kinetics, it follows from Table 1 that both σ and P will drop over time: $F(X)\downarrow 0$ for $X\uparrow 1$.

The second issue is about the reaction regimes in case a traveling hydration front can develop, $Da_b > 1$. There will be at most three periods in the reaction process: a rising rate period (RRP) with a duration Δt_{RRP}, a constant rate period (CRP) with a length Δt_{CRP}, and a falling rate period (FRP) with a time span Δt_{FRP}. A schematic overview of the analysis is presented in Fig. 4. Below, each reaction phase will be discussed in more detail.

During the RRP phase water vapor has spread through the particle

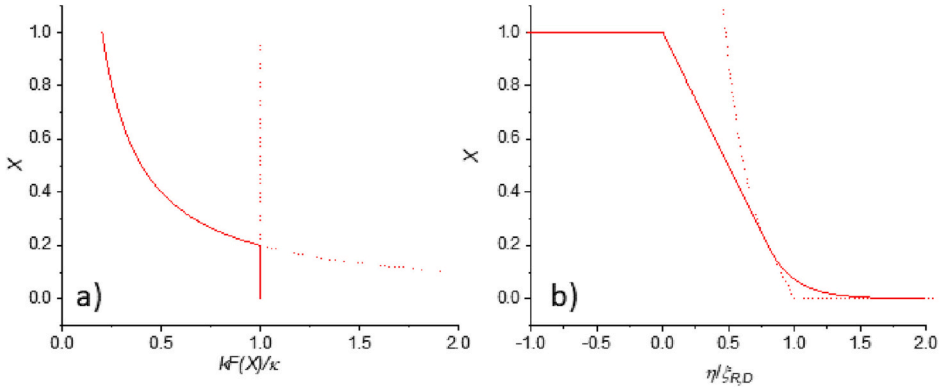

Fig. 3. The front shape for the CR-DLR_1 model at $Da_p = 5$: a) the reaction rate in relation to the conversion, b) the resulting front shape. At low conversion the rate is constant and not transport limited. At higher conversion diffusion limits the reaction process. The constant rate regime introduces an exponential tail at the leading edge of the hydration front.

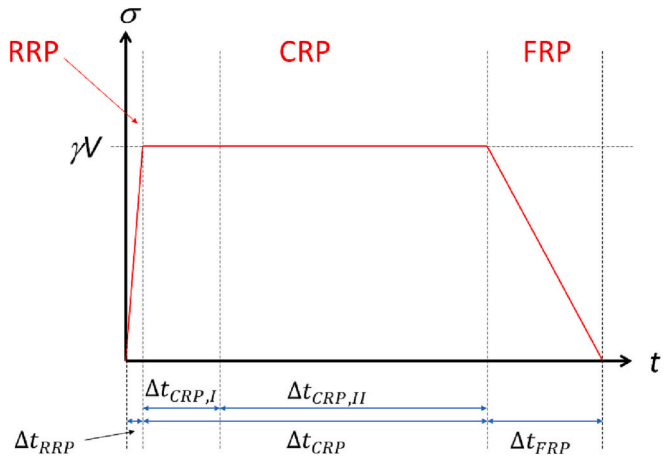

Fig. 4. A schematic overview of the different reaction rate phases in a finite sized particle bed: rising rate (RRP), constant rate (CRP) and falling rate (FRP).

bed as a prerequisite for hydration. At the start of the process $\sigma(0) = 0$ as $c(z,0) = c_{eq}$. During the RRP phase water vapor redistributes through the system resulting in $c(z,t) \geq c_{eq}$ and $\sigma(t) > 0$. At the end of the RRP as a quasi-steady state is reached the net influx of water vapor equals the global reaction rate, and $\sigma(\Delta t_{RRP}) = \phi_b U \Delta c$ (see Eq. (43)). The advective timescale can be used as an upper bound: $\Delta t_{RRP} \leq L/U$. Using typical values for the air velocity (U = 0.01–1 m/s) and the bed length ($L = 1$ m), one finds that $\Delta t_{RRP} \leq 1 - 100$ s.

In the CRP period itself the reaction rate is constant. As $c(0,t) - c(L,t) = c_0 - c_{eq} = \Delta c$, one finds that Eq. (43) equals

$$\sigma(t) = \phi_b U \Delta c = \gamma V \tag{46}$$

This period can be split into two phases: I) the front is developing $X(0,t) < 1$ and II) the developed front travels through the bed till its leading edge arrives at $z = L$ ($X(0,t) = 1$ and $X(L,t) = 0$). The duration of the CRP phase is given by.

$$\Delta t_{CRP} = \Delta t_{CRP,I} + \Delta t_{CRP,II} \approx t_1 + \frac{L - W}{V} \tag{47}$$

Here $\Delta t_{CRP,I}$ [s] and $\Delta t_{CRP,II}$ [s] refer to the periods that the front develops and that the front travels, respectively. The traveling time of a fully developed front $\Delta t_{CRP,II}$ is simply the ratio between the length it can travel, $L - W$, and its velocity V. Further, $\Delta t_{CRP,I} \approx t_1$, which is the time to reach full hydration at $z = 0$, which can be estimated from the particle reaction kinetics. Note that particles just at entrance of the bed ($z = 0$) are always subject to a constant water vapor concentration c_0.

By solving Eq. (4) for the different DLR models (see Table 1), equations for t_1 can be obtained. For details we refer to the literature [16].

$$\Delta t_{CRP} \approx \frac{r^2(\beta - \alpha)\rho}{2nD_p \Delta c} + \frac{L - W}{V} \tag{48}$$

Here $n = 1, 2, 3$ refers to the type of DLR-model. As a salt hydrate particle at the entrance of the bed, $z = 0$, is subject to a constant water vapor concentration, $c(0,t) - c_{eq} = \Delta c$, the particle's hydration is fully determined by its intrinsic reaction kinetics. By using Eq. (8), Eq. (12). Eq. (36), Eq. (44), we can rewrite Eq. (48).

$$\Delta t_{CRP} \approx \frac{L}{V}\left(1 - \frac{1}{Da_b}\left[1 - \frac{1}{2nC_n}\right]\right) \tag{49}$$

Here the term L/V is the time it takes a fully developed front to travel a distance L. The term $Da_b^{-1}(1 - 1/2nC_n)$ corrects for the finite size of the front. According to this equation the constant rate period vanishes at $Da_b = 1 - 1/2nC_n$, which is inline with the notion that below $Da_b \sim 1$ the hydration process is reaction limited. From this we can immediately conclude Δt_{CRP} is orders of magnitude longer than Δt_{RRP} as $\phi_b \Delta c/\gamma \ll 1$ (see Fig. 6), and that the RRP phase can be neglected. This also means that the transition from the CRP to the FRP occurs approximately at $t^* \approx \Delta t_{CRP}$.

The duration of the falling rate period Δt_{FRP} is the time needed for the front to travel over distance of its own width.

$$\Delta t_{FRP} = \frac{W}{V} = \frac{L}{V}\left(\frac{1}{Da_b}\right) \tag{50}$$

In the derivation we used Eq. (44). Note that the duration of the FRP phase is determined by the reaction kinetics of the particle.

In Fig. 5 we have plotted the fraction of time that a bed hydrates with a constant rate as function of Da_b for the different DLR models. From this it can be concluded that irrespectively of the model, $Da_b > 4$ to make sure that the hydration rate is constant for a significant fraction of the whole reaction time.

5. Quantification of hydration fronts and implications for finite sized bed

5.1. Front speed

First the speed of the hydration front V, Eq. (10), will be quantified for different beds of different salt types: $CuCl_2$, K_2CO_3, LiCl, $MgCl_2$, $SrBr_2$ and $SrCl_2$. All salts, except $CuCl_2$, are widely investigated as potential storage material in TCES devices. As $\phi_b \Delta c/\gamma$ is the key parameter for calculating the ratio V/U, values for γ and ϕ_b and $\Delta c = c - c_{eq}$ are needed.

Here we set $\phi_b = 0.5$. The selected value for ϕ_b is within the range for packed beds of particles, as in practice ϕ_b varies at most between 0.35 and 0.55 for random packs of particles [47,48]. As $\phi_b \Delta c/\gamma$ is proportional to $\phi_b/(1 - \phi_b)$, see Eq. (8), variation of the bed porosity between 0.35 and 0.55 leads to a variation of $\phi_b/(1 - \phi_b)$ between 0.5 and 1.2. To obtain values for the parameter γ data on the crystal densities of the starting phases, ρ_α, have been collected, see Table 3. For ρ_α and ρ_β are crystallographic densities were obtained from SpringerMaterials [49]. The particle porosity has been set to its lower limit $\phi_p = 1 - \rho_\beta/\rho_\alpha$, which implies the assumption that upon dehydration ($\beta \rightarrow \alpha$) the particle changes from a hardly porous to a porous particle without changing its volume. The resulting variation of γ is relatively limited, between $7.67 \cdot 10^3$ and $1.72 \cdot 10^4$ mol/m^3, which is understandable as this parameter reflects the water density in a salt hydrate. To calculate $\Delta c = c_0 - c_{eq}$ values for c_0 and c_{eq} are needed. We have chosen $c_0 = 0.51$ mol/

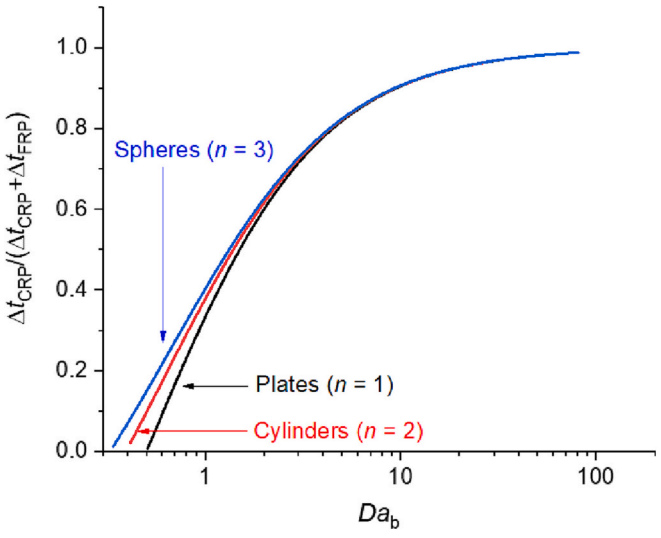

Fig. 5. The fraction of time that a finite bed of salt hydrate particles has constant hydration rate: the CRP (constant rate period).

Table 3
Input parameters for calculating the speed of the hydration front for hydration transitions of different salt hydrates.

Salt	α	β	ρ_α [mol/m3]	ρ_β [mol/m3]	ϕ_p	γ [mol/m3]	H [kJ/mol]	S [J/mol K]
$CuCl_2$	0	2	$2.52{\cdot}10^4$	$1.49{\cdot}10^4$	0.41	$1.49{\cdot}10^4$	60.7	151
K_2CO_3	0	1.5	$1.76{\cdot}10^4$	$1.32{\cdot}10^4$	0.25	$9.89{\cdot}10^3$	63.3	153
LiCl	0	1	$4.81{\cdot}10^4$	$2.91{\cdot}10^4$	0.39	$1.46{\cdot}10^4$	60.0	142
$MgCl_2$	2	4	$1.45{\cdot}10^4$	$9.71{\cdot}10^3$	0.33	$9.71{\cdot}10^3$	64.6	140
$MgCl_2$	4	6	$9.71{\cdot}10^3$	$7.67{\cdot}10^3$	0.21	$7.67{\cdot}10^3$	56.7	132
$SrBr_2$	1	6	$1.46{\cdot}10^4$	$6.86{\cdot}10^3$	0.53	$1.72{\cdot}10^4$	61.0	154
$SrCl_2$	1	2	$1.65{\cdot}10^4$	$1.39{\cdot}10^4$	0.16	$6.96{\cdot}10^3$	58.0	126
$SrCl_2$	2	6	$1.39{\cdot}10^4$	$7.39{\cdot}10^3$	0.47	$1.48{\cdot}10^4$	53.4	142

m^3, which corresponds to a saturated water vapor of 12 mbar at 10 °C (a widely used value in TCES applications). The equilibrium vapor density c_{eq} is calculated with the help of Eq. (3) with values of H and S as input. The value for H and S, as given in Table 3, have been obtained by fitting experimental data on the pressure-temperature line of the hydration transition for the different salt [50–53].

Predictions for the ratio of the front and air velocities V/U as a function of temperature are shown in Fig. 6. The figure demonstrates three important issues. First, irrespectively of the salt type, the kinetics of the hydration front is always orders of magnitude lower than the air velocity: $V \ll U$. This is not surprising as the hydration involves the absorption of a lot of water per volume from the air phase that contain only small amounts, which is reflected by the parameter $\phi_b \Delta c/\gamma$. So, a lot of water vapor must be advected to the reaction front to move this front. Practically this means that Eq. (12) can safely be used for prediction of the hydration front velocity. Differences between the different salts are a direct consequence of the parameter $\phi_b \Delta c/\gamma$. Effectively the front speed follows from mass conservation issues: the balance between the water vapor density $\phi_b \Delta c$ and the absorption capacity of the salt γ.

The second observation is about the temperature dependency of V. The curves in Fig. 6 show that the front velocity is very sensitive to temperature and goes to 0 at a specific temperature T^* [K] that is salt dependent. Given the definition of $\phi_b \Delta c/\gamma$ both the temperature dependency as the point T^* is solely determined by the phase diagram of the specific salt (the pressure-temperature line of the phase transition) as can be seen in Eq. (3). At T^* the input vapor density matches the equilibrium water density of the salt: $c_0 = c_{eq}(T^*)$.

A third feature visible in Fig. 6 is related to the magnitude of the ratio

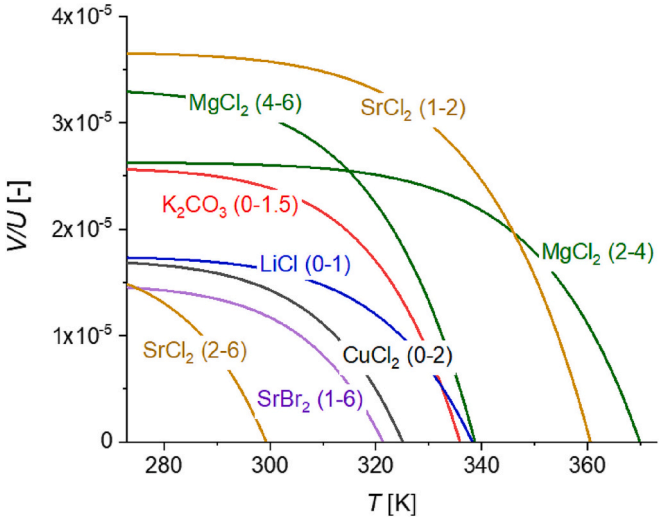

Fig. 6. The ratio between the velocity of the hydration front V and the air speed U for different hydration transitions as a function of temperature. The numbers behind the chemical formula's (i.e. $MgCl_2$ (2–4)) refer the hydration states before and after the transition. The calculations have been performed with inlet water vapor concentration of $c_0 = 0.51$ mol/m^3, which corresponds to a saturated water vapor of 12 mbar at 10 °C.

V/U. The spread in values of V/U ($5.0{\cdot}10^{-6}$–$3.6{\cdot}10^{-5}$ at 290 K) greatly exceeds the spread in values of γ ($6.67{\cdot}10^3$–$1.72{\cdot}10^4$ mol/m^3). This further illustrates that the phase behavior of a specific salt strongly impacts the front dynamics.

In the calculations, shown in Fig. 6, the porosities of the bed ϕ_b and of the salt particle ϕ_p was fixed. Now it has been shown that the front velocity for realistic systems can be approximated with Eq. (12), the impact of porosity can be demonstrated by calculating the factor $\phi_b/(1-\phi_b)\left(1-\phi_p\right)$. Note that this factor includes all porosity contributions in the parameter $\phi_b \Delta c/\gamma$. The factor $\phi_b/(1-\phi_b)\left(1-\phi_p\right)$ is plotted in Fig. 7 for realistic values of the porosities of packed beds, $0.35 \leq \phi_b \leq 0.55$, and a K_2CO_3 particle pressed from a powder. Note that for K_2CO_3 $\phi_p = 0.25$ is the lowest porosity a particle in the α-phase can have, see Table 3. Clearly, the hydration front moves faster with increasing porosities of the bed and the particles itself. High porosities mean low solid densities, and therefore a low absorption capacity for water (low values of γ).

5.2. Front width

As shown in Section 3, ξ_R is the length scale characterizing the extent of the hydration front. Furthermore, it has been found that the front zone has a well-defined width W in case the particle reaction kinetics is diffusion limited (the DLR models), see Fig. 2 and Table 2. Here W will be quantified for parameters relevant for TCES applications. Quantification will be done with the DLR particle models for reaction kinetics (see Table 1).

From the equations for W and $\xi_{R,D}$ it follows that salt type has no direct influence on the extend of the hydration front. The particle

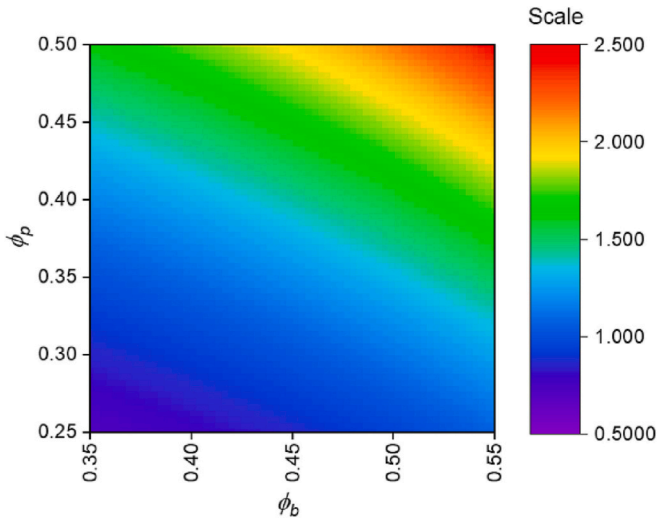

Fig. 7. The impact of the bed and particle porosity (ϕ_b and ϕ_p) on the speed of the hydration front. The color coding refers to the scaling parameter $\phi_b/(1-\phi_b)\left(1-\phi_p\right)$.

properties that matter are the size r, and microstructure as reflected in the value of D_p. In this section we will discuss the impact of air velocity, particle size, particle shape and water vapor diffusivity.

In all our calculation we will set $\phi_b = 0.5$, which is a representative value for the bed (see discussion in Section 5.1). We will vary the air flow speed U from 0.01 to 1 m/s, as reported values for TCES are 0.1–1 m/s. D_p will be varied between 0.1 and 10 mm^2/s, which can be justified as follows. First, K_2CO_3 particles (in the hydrate phase) with porosities varying between 0.01 and 0.25, have D_p values varying between 0.1 and 1.75 mm^2/s. Furthermore, an upper bound for D_p is the water vapor diffusivity in air that is 24 mm^2/s at 20 °C. The particle radius/size, r, will be varied between 0.1 and 10 mm. Presently, it is believed that for optimal output of advective driven TCES reactors the particles should be millimeter sized. Beds of submillimeter particles have low bed permeabilities and demand a high input power for driving flow. The outcomes of the calculations are shown in Fig. 8. Below we subsequently discuss the influence of velocity, the role of the vapor diffusivity in the salt particle and the particle size. Assuming that in TCES application reactor dimensions are typically in the range of 0.1–1 m, we will compare predictions for W with a length scale of 10 cm.

First, the influence of the air velocity was studied at $r = 1.5$ mm and $D_p = 1$ mm^2/s, see Fig. 8a. As already discussed, the influence of the particle shape, n, on the front width W is significant: i.e. while for spherical particles $W \approx 56$ cm at $U = 1$ m/s, the front width in case of plate-like particles is about 225 cm. To bring down the front width below the 10 cm, U must be below 0.05, 0.1 and 0.2 m/s for plates, cylinders, and spheres, respectively.

Secondly, the impact of the water vapor diffusivity in the particle is shown in Fig. 8b. In the calculations $U = 1$ m/s and $r = 1.5$ mm. Note that D_p is strongly connected with structural properties of the particle such as porosity and tortuosity. For $U = 1$ m/s and $r = 1.5$ mm front widths below the 10 cm are not expected for plate-like particles as the theoretical value for D_p exceeds its upper bound: the water vapor diffusivity in pure air, 24 mm^2/s at 20 °C. For cylinders and spheres D_p should be above 9.1 and 5.5 mm^2/s, respectively.

Third, the parameter r characterizing the size of the salt hydrate particle is varied, while $U = 1$ m/s and $D_p = 1$ mm^2/s, see Fig. 8c. The front width steeply rises with the particle size as vapor diffusion into the particle slows down. Salt particles need to be submillimeter sized to push W below the 10 cm at the chosen values for U and D_p.

Finally, some words must be spent on the impact of temperature on the front shape and width. It follows from Eq. (36) and Eq. (19) that temperature only impacts W via the D_p. The temperature influence D_p via the diffusivity of water vapor in air D_{air}, see Eq. (5). As D_{air} increases from 24 mm^2/s at 20 °C to 40 mm^2/s at 100 °C, one can conclude that W will only decrease with a factor 1.7 with a temperature increase from 20 to 100 °C. From this we can conclude that the front shape and width W are far less sensitive to changes in temperature than the front speed V. Note that this conclusion only holds for particle beds subject to a homogeneous temperature distribution (isothermal particle beds). The impact of temperature gradients cannot be analyzed within the framework of the presented model, as the time evolution of the temperature field should be modelled explicitly.

5.3. Hydration in finite sized beds

To assess if hydration in a finite particle bed is reaction limited or transport limited, the value $Da_b = L/W$ (see Eq. (44)) must be assessed. Here we can refer to the previously discussed values of the front width W, see Fig. 8. For a typical set of parameters ($U = 1$ m/s, $D_p = 1$ mm^2/s and $r = 1.5$ mm), one finds that W equals 2.50, 0.93 and 0.56 m for plate-like particles (DLR_1), cylinders (DLR_2), and spheres (DLR_3), respectively. This means hydration fronts and a CRP-phase ($Da_b > 1$) will only occur in particle beds of several meters. The only way to stimulate front formation is by reducing the airflow U or by increase the reaction via decreasing the particle size r or increasing the diffusivity D_p.

In practice a high and constant global reaction rate σ are wanted as that determines the power output of a TCES reactor. The present analysis makes clear that satisfying both requirements is a major challenge for particle beds of sizes between 10 and 100 cm in case of millimeter sized salt hydrate particles.

6. Temperature gradients

6.1. Theory

Finally, we investigate how temperature gradients, induced by the exothermic nature of the hydration reaction, influence key properties for like a) the temperature lift $\Delta T \equiv T_{out} - T_{in}$ [K] achieved by hydration, b) the speed of the hydration front V and c) the power output per area $P = H\sigma$. T_{in} and T_{out} [K] are the input and output temperatures, respectively. We limit the discussion to the case that a traveling hydration front has developed: $W/L \ll 1$. The section starts with a discussion of the essential equations, followed by quantification for the same salts as discussed in Section 5.

The temperature lift ΔT can be found by equating the heat production per area during the hydration reaction,

$$P = \phi_b U \Delta c H = \phi_b U \left(c_0 - c_{eq}(T_{out})\right) H \tag{51}$$

and the net heat flux due to advection,

$$P = \phi_b U C_{air} \rho_{air} \Delta T = \phi_b U C_{air} \rho_{air} (T_{out} - T_{in}) \tag{52}$$

resulting in

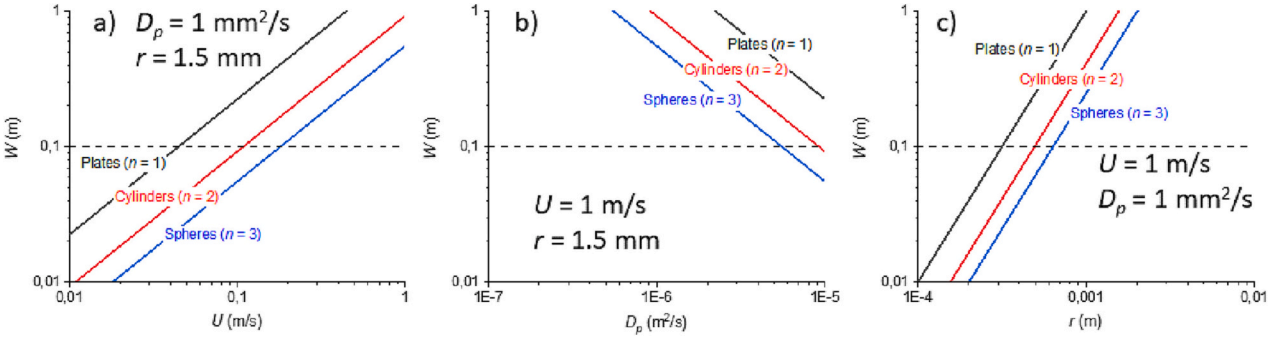

Fig. 8. Predictions for the front width W for DLR-type reaction kinetics. Predictions for plate-like (black), cylinderical (red) and spherical particles (blue) are shown. The horizontal dotted line refers to $W = 10$ cm. Three parameter variations are shown: the influences of a) the air velocity U for $D_p = 1$ mm^2/s and $r = 1.5$ mm, b) the water vapor diffusivity in the salt hydrate particle D_p for $r = 1.5$ mm and $U = 1$ m/s, and c) the particle dimension r for $U = 1$ m/s and $D_p = 1$ mm^2/s. (For interpretation of the references to color in this figure legend, the reader is referred to the web version of this article.)

$$c_0 - c_{eq}(T_{out}) = \frac{C_{air}\rho_{air}}{H}(T_{out} - T_{in}) \quad (53)$$

Note that $c_{eq}(T_{out})$ couples with the output temperature in a non-linear fashion, see Eq. (3). C_{air} and ρ_{air} are the molar heat capacity and molar density of air, respectively.

Solving the latter equation not only results in ΔT, but also gives Δc, which allows calculating the speed of the hydration front V via Eq. (10) and the power output P. Calculations were performed for the same salts as discussed in Section 5, using the parameters characterizing the salt particles as listed in Table 3. As in Section 5 we have set $c_0 = 0.51$ mol/m^3 (a water vapor of 12 mbar generated at 10 °C). In our calculations we have used $\rho_{air} = p^0/RT_{out}$ and $C_{air} = 29.12$ J/mol K, which are typical values for air at 1 atm and 25 °C. Calculations for P were done with $\phi_b U = 1$ m/s, and thus the outcomes are easily scalable for other air velocities. Results will be discussed in the following subsections.

6.2. Temperature lift and power output

As P is proportional to ΔT, we will discuss both properties simultaneously. In Fig. 9 results are shown for varying values of T_{in}.

The temperature lifts over particles beds strongly depend on the salt type, see Fig. 9a. According to Eq. (53) the nature of the salts enters via the parameters H and c_{eq} (T_{out}), where the latter depend H and S (Eq. (3)). Whereas H and S only vary 10 kJ/mol and 10 J/mol K, see Table 3, the non-linear nature of c_{eq} makes ΔT very sensitive to these small variations (note that $RT \sim 2.5$ kJ/mol).

At low values of T_{in} the temperature lift approaches a maximal value for the hydration transitions $MgCl_2$ (2–4) and $SrCl_2$ (1–2). This can be understood as follows. The values for $c_{eq}(T_{out})$ are low compared to c_0, and $\Delta T \approx Hc_0/C_{air}\rho_{air}$ (see Eq. (53)), which no longer depends on temperature gradients in the system. For the previously used typical parameter set ($c_0 = 0.51$ mol/m^3, $\rho_{air} = p^0/RT$, and $C_{air} = 29.12$ J/mol K) one can show that the maximal achievable temperature lift ΔT varies between 21 and 28 K for reaction enthalpies H varying between 50 and 65 kJ/mol. Note that the majority of the hydration transitions have enthalpies within in this range of values [6–8]. Therefore, a major increase in the maximal achievable value of ΔT can only be achieved by working at higher water vapor pressures resulting higher values of c_0.

Finally, we briefly discuss the power output as plotted in Fig. 9b. The curves for all salts nicely follow the behavior of the temperature lift ΔT, which is a direct consequence of Eq. (52). The salt type impacts ΔT and thereby P. Also, P approaches a maximal value for the hydration transitions $MgCl_2$ (2–4) and $SrCl_2$ (1–2), which is again a consequence of the fact that $c_{eq}(T_{out}) \ll c_0$. In this case Eq. (51) reduces to $P \approx \phi_b U c_0 H$, which sets an upper bound for the power. As H does not vary a lot between the various salts, one does not expect that the maximal achievable power varies lot between salts.

6.3. Front speed

Velocities of the hydration front V are plotted as a function of the input temperature in Fig. 10. Comparing these non-isothermal velocities with the isothermal ones, see Fig. 6, leads to the following observations: 1) in both cases the front velocities vanish at the same temperature, 2) at low temperatures the velocities in both cases converge to similar values, and 3) temperature gradients suppress the motion of the hydration front at intermediate temperatures. These observations can all be explained based on the influence of a temperature gradients on the concentration

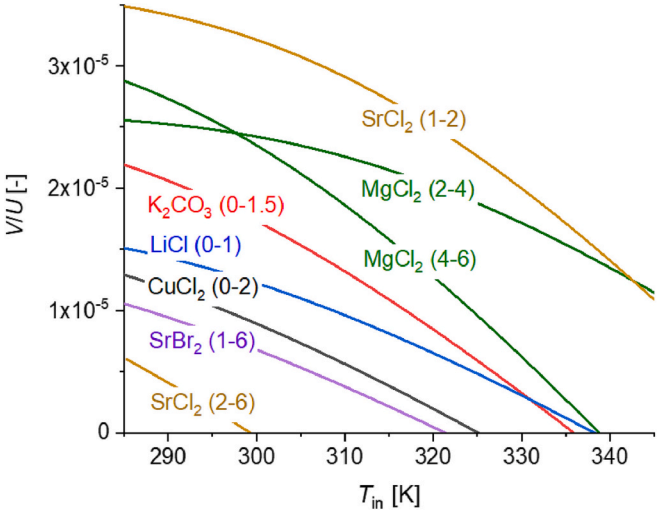

Fig. 10. The ratio between the velocity of the hydration front V and the air speed U for different hydration transitions as a function of temperature. The numbers behind the chemical formula's (i.e. $MgCl_2$ (2–4)) refer the hydration states before and after the transition. The calculations have been performed with an inlet vapor concentration of $c_0 = 0.51$ mol/m^3, which corresponds to a saturated water vapor of 12 mbar at 10 °C.

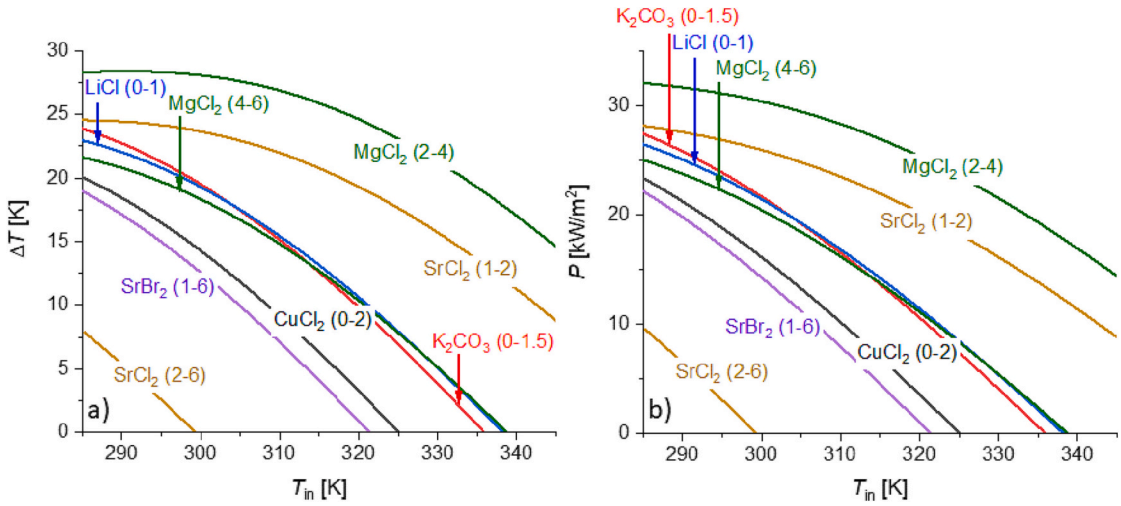

Fig. 9. Hydration characteristics of beds salt hydrate particles: a) temperature lift ΔT, and b) the power output per areal P at $\phi_b U = 1$ m/s. The numbers behind the chemical formula's (i.e. $MgCl_2$ (2–4)) refer the hydration states before and after the transition. The calculations have been performed with an inlet vapor concentration of $c_0 = 0.51$ mol/m^3, which corresponds to a saturated water vapor of 12 mbar at 10 °C.

drop Δc, which is a key parameter for V, Eq. (10). First, velocities with and without temperature gradients drop to zero at the same temperatures, because temperature gradients vanish at this temperature, see Fig. 9a. Secondly, Eq. (10) explains why in the presence of temperature gradients the values for V converge to similar values as in the isothermal case. At low temperatures $c_0 \gg c_{eq}$ and $\Delta c \approx c_0$, which has the consequence that even in the presence of temperature gradients the front velocity decouples from the existing temperature gradient. The third observation, slowing down of the hydration front due to the presence of temperature gradients, can be understood as follows. The temperature rise of the output temperature increases c_{eq} and squeezes Δc, and thereby reduces the fronts speed.

7. Conclusions

Isothermal hydration in packed beds has been studied in view of thermochemical energy storage (TCES). The focus was on packed beds of millimeter sized salt hydrate particles. It was shown that in case of millimeter sized particles, bed hydration can be modelled as an advection-reaction process, and vapor diffusion and dispersion can be neglected. Predictions have been made for the speed and width of traveling hydration fronts through infinite particle beds. The implications for finite sized beds have been assessed based on a type I Damköhler number Da_b: the ratio between the system size L and the front width W.

The speed at which the hydration front travels through the particle bed V, turns out to be independent of the reaction kinetics of the individual salt hydrate particles but increases with the air velocity U and ratio between the water content in air and the absorbed amount of water $\phi_b \Delta c/\gamma$, see Eq. (10). Estimates done for widely studied salt hydrates indicate that the speed of the hydration front is typically five orders of magnitude lower than the air velocity in case the system is far from equilibrium $(c_0 \gg c_{eq})$: $V/U \sim 10^{-5}$. Close to equilibrium $(c_0 \sim c_{eq})$, the hydration front slows down to very low speeds, see Fig. 6.

Contrary to the front speed, the front width and shape are strongly linked with the particle reaction kinetics. The front width W increases with the air velocity U and decreases with the kinetic constants for the particle reaction. In case of diffusion limited hydration kinetics inside the salt hydrate particle, W increases with the particle size and decreases with the water vapor diffusivity inside the particle. The reaction pathway as reflected by $F(X)$, see Eq. (4), fully determines the shape of the hydration front. As such front shapes can be predicted with a function $F(X)$ extracted from a model for particle hydration or experimentally determined hydration kinetics (i.e. with TGA).

For relevant TCES conditions and millimeter sized salt hydrate particles it was shown that the hydration front has a width in the order of 10–100 cm. Therefore, hydration fronts will only develop when the sizes of the particle beds become several meters ($Da_b > 1$).

We have shown that the hydration kinetics of a finite sized particle bed will have three distinct phases: a rising rate period (RRP), a constant rate period (CRP) and a falling rate period (FRP). The duration of the RRP phase is negligible compared to the lengths of the CRP and FRP phases as it is related to water vapor redistribution towards a quasi-steady state situation. The FRP period sets in when the leading edge of the hydration front reaches the end of the particle bed. The duration of this phase is equal to the time it takes the front to travel a distance equal to its own width: W/V. The importance of the CRP phase increases with increasing Da_b. Based on our estimations for the front width, see Fig. 8, a significant constant rate period (CRP) leading to a constant power output is only expected for TCES reactors with bed lengths of several meters. This stresses the need for salt hydrate particles with faster hydration kinetics on the particle level.

Furthermore, we have analyzed the impact of temperature gradients on properties like temperature lift ΔT, front velocity V, and power output per area P in the case that the front width is much smaller than the bed size ($W/L \ll 1$). These variables could be extracted without solving the full equations for the shape of the hydration front itself. At low input temperatures V decouples from the temperature gradients and becomes equal to the isothermal predictions. Furthermore, the temperatures at which the front speed vanish are also independent of temperature gradients. Our estimates of the output power P and ΔT give theoretical upper bounds for the performance of TCES based on salt hydrate bed. These upper bounds do not vary a lot between different salts as the reaction enthalpy for salt hydration does not vary a lot between salts.

Finally, we conclude that the power and the beauty of the presented model is in its ability to come up with simple relationships for properties like the front speed, front width, and global hydration rates. These relationships facilitate developing TCES reactors by supplying simple design criteria without the need of complex computational models.

Although temperature gradients and finite size effects have been analyzed and discussed, future steps will be the addition of energy balance equations for studying the precise impact of temperature gradients on the shape and width of hydration fronts, and a more quantitative analysis of finite size effects.

CRediT authorship contribution statement

Henk Huinink: Conceptualization, Methodology, Writing – original draft, Investigation. **Stan de Jong:** Conceptualization, Writing – review & editing, Investigation. **Vera Houben:** Conceptualization, Writing – review & editing, Investigation.

Declaration of competing interest

The authors declare that they have no known competing financial interests or personal relationships that could have appeared to influence the work reported in this paper.

Data availability

Data will be made available on request.

Acknowledgments

This project has received funding from the European Unions Horizon 2020 Research and Innovation Program under grant agreement No 869810. This work reflects only the author's view. The European Commission is not responsible for any use that may be made of this information.

References

[1] R.U. Cooke, I.J. Smalley, Salt weathering in deserts, Nature 220 (1968) 1226–1227, https://doi.org/10.1038/2201226a0.
[2] E.M. Winkler, E.J. Wilhelm, Salt burst by hydration pressures in architectural stone in urban atmosphere, Geol. Soc. Am. Bull. 81 (2) (1970) 567–572, https://doi.org/10.1130/0016-7606(1970)81[567:SBBHPI]2.0.CO;2.
[3] A.S. Goudie, H.A. Viles, Salt Weathering Hazards, 1st ed., Wiley, 1997.
[4] R.J. Flatt, G.W. Scherer, Hydration and crystallization pressure of sodium sulfate: a critical review, MRS Online Proc. Libr. 712 (2001) 22, https://doi.org/10.1557/PROC-712-II2.2.
[5] M. Steiger, K. Linnow, H. Juling, G. Gülker, A. El Jarad, S. Brüggerhoff, D. Kirchner, Hydration of $MgSO_4 \cdot H_2O$ and generation of stress in porous materials, Crystal Growth Des. 8 (1) (2008) 336–343, https://doi.org/10.1021/cg060688c.
[6] K.E. N'Tsoukpoe, T. Schmidt, H.U. Rammelberg, B.A. Watts, W.K.L. Ruck, A systematic multi-step screening of numerous salt hydrates for low temperature thermochemical energy storage, Appl. Energy 124 (2014) 1–16, https://doi.org/10.1016/j.apenergy.2014.02.053.
[7] P.A.J. Donkers, L.C. Sögütoglu, H.P. Huinink, H.R. Fischer, O.C.G. Adan, A review of salt hydrates for seasonal heat storage in domestic applications, Appl. Energy 199 (2017) 45–68, https://doi.org/10.1016/j.apenergy.2017.04.080.
[8] M. Richter, E.-M. Habermann, E. Siebecke, M. Linder, A systematic screening of salt hydrates as materials for a thermochemical heat transformer, Thermochim. Acta 639 (2018) 136–150, https://doi.org/10.1016/j.tca.2017.06.011.

[9] R.-J. Clark, A. Mehrabadi, M. Farid, State of the art on salt hydrate thermochemical energy storage systems for use in building applications, J. Energy Storage 27 (2020), 101145, https://doi.org/10.1016/j.est.2019.101145.

[10] W. Li, J.J. Klemes, Q. Wang, M. Zeng, Salt hydrate-based gas-solid thermochemical energy storage: current progress, challenges and perspectives, Renew. Sust. Energ. Rev. 154 (2022), 111846, https://doi.org/10.1016/j.rser.2021.111846.

[11] T. Li, R. Wang, J.K. Kiplagat, Y.T. Kang, Performance analysis of an integrated energy storage and energy upgrade thermochemical solid–gas sorption system for seasonal storage of solar thermal energy, Energy 50 (2013) 454–467, https://doi.org/10.1016/j.energy.2012.11.043.

[12] T.X. Li, R.Z. Wang, T. Yan, T.F. Ishugah, Integrated energy storage and energy upgrade, combined cooling and heating supply, and waste heat recovery with solid–gas thermochemical sorption heat transformer, Int. J. Heat Mass Transf. 76 (2014) 237–246, https://doi.org/10.1016/j.ijheatmasstransfer.2014.04.046.

[13] A.I. Shkatulov, J. Houben, H. Fischer, H.P. Huinink, Stabilization of K_2CO_3 in vermiculite for thermochemical energy storage, Renew. Energy 150 (2020) 990–1000, https://doi.org/10.1016/j.renene.2019.11.119.

[14] R.-J. Clark, M. Farid, Experimental investigation into the performance of novel $SrCl_2$-based composite material for thermochemical energy storage, J. Energy Storage 36 (2021), 102390, https://doi.org/10.1016/j.est.2021.102390.

[15] R. Fisher, Y. Ding, A. Sciacovelli, Hydration kinetics of K_2CO_3, $MgCl_2$ and vermiculite-based composites in view of low temperature thermochemical energy storage, J. Energy Storage 38 (2021), 102561, https://doi.org/10.1016/j.est.2021.102561.

[16] J. Aarts, S. de Jong, M. Cotti, P. Donkers, H. Fischer, O. Adan, H. Huinink, Diffusion limited hydration kinetics of millimeter sized salt hydrate particles for thermochemical heat storage, J. Energy Storage 47 (2022), 103554, https://doi.org/10.1016/j.est.2021.103554.

[17] A.H. Abedin, M.A. Rosen, Closed and open thermochemical energy storage: energy- and exergy-based comparisons, Energy 41 (1) (2012) 83–92, https://doi.org/10.1016/j.energy.2011.06.034.

[18] B. Michel, P. Neveu, N. Mazet, Comparison of closed and open thermochemical processes, for long term thermal energy storage applications, Energy 72 (2014) 702–716, https://doi.org/10.1016/j.energy.2014.05.097.

[19] A. Fopah-Lele, C. Rohde, K. Neumann, T. Tietjen, T. Rönnebeck, K.E. N'Tsoukpoe, T. Osterland, O. Opel, W.K.L. Ruck, Lab-scale experiment of a closed thermochemical heat storage system including honeycomb heat exchanger, Energy 134 (2016) 225–238, https://doi.org/10.1016/j.energy.2016.08.009.

[20] A.-J. de Jong, L. van Vliet, C. Hoegaerts, M. Roelands, R. Cuypers, Thermochemical heat storage – from reaction storage density to system storage density, Energy Procedia 91 (2016) 128–137, https://doi.org/10.1016/j.egypro.2016.06.187.

[21] J. Houben, L. Sögütoglu, P. Donkers, H. Huinink, O. Adan, K_2CO_3 in closed heat storage systems, Renew. Energy 166 (2020) 35–44, https://doi.org/10.1016/j.renene.2020.11.119.

[22] H. Zondag, B. Kikkert, S. Smeding, R. de Boer, M. Bakker, Prototype thermochemical heat storage with open reactor system, Appl. Energy 109 (2013) 360–365, https://doi.org/10.1016/j.apenergy.2013.01.082.

[23] F. Marias, P. Neveu, G. Tanguy, P. Papillon, Energy 66 (2014) 757–765, https://doi.org/10.1016/j.energy.2014.01.101.

[24] J. Houben, P.A.J. Donkers, H.P. Huinink, S.J.F. Erich, O.C.G. Adan, M.Z. Siddiqui, WO2019038292 – closed cycle thermal energy storage system using thermochemical material. https://patentscope.wipo.int/search/en/detail.jsf?docId=WO2019038292, 2019.

[25] G. Balasubramanian, M. Ghommem, M.R. Hajj, W.P. Wong, J.A. Tomlin, I.K. Puri, Modeling of thermochemical energy storage by salt hydrates, Int. J. Heat Mass Transf. 53 (2010) 5700–5706, https://doi.org/10.1016/j.ijheatmasstransfer.2010.08.012.

[26] A.A. Hawwash, S. Mori, K. El Feky, H. Hassan, Numerical study for open reactor design using salt hydrate, IOP Conf. Ser. Earth Environ. Sci. 322 (2019), 012021, https://doi.org/10.1088/1755-1315/322/1/012021.

[27] G. Michel, N. Mazet, S. Mauran, D. Stitou, J. Xu, Thermochemical process for seasonal storage of solar energy: characterization and modeling of a high density reactive bed, Energy 47 (1) (2012) 553–563, https://doi.org/10.1016/j.energy.2012.09.029.

[28] T. Nagel, S. Beckert, C. Lehmann, R. Gläser, O. Kolditz, Multi-physical continuum modles for thermochemical heat storage and transformation in porous media and powder beds – a review, Appl. Energy 178 (2016) 323–345, https://doi.org/10.1016/j.apenergy.2016.06.051.

[29] A. Mahmoudi, P.A.J. Donkers, K. Walayat, B. Peters, M. Shahi, A thorough investigation of thermochemical heat storage system from particle to bed scale, Chem. Eng. Sci. 246 (2021), 116877, https://doi.org/10.1016/j.ces.2021.116877.

[30] N. Mikos-Nuzkiewicz, P. Furmanski, P. Lapka, A mathematical model of charging and discharging processes in a thermochemical energy storage reactor using the hydrated potassium carbonate as a thermochemical material, Energy 263A (2023), 125642, https://doi.org/10.1016/j.energy.2022.125642.

[31] X. Luo, W. Li, Q. Wang, M. Zeng, Numerical investigation of a thermal energy storage system based on the serpentine tube reactor, J. Energy Storage 56 (B) (2022), 106071, https://doi.org/10.1016/j.est.2022.106071.

[32] F. Birkelbach, M. Deutsch, A. Werner, The effect of the reaction equilibrium on the kinetics of gas-solid reactions — a non-parametric modeling study, Renew. Energy 152 (2020) 300–307, https://doi.org/10.1016/j.renene.2020.01.033.

[33] J. Stengler, I. Bürger, M. Linder, Thermodynamic and kinetic investigations of the $SrBr_2$ hydration and dehydration reactions for thermochemical energy storage and heat transformation, Appl. Energy 277 (2020), 115432, https://doi.org/10.1016/j.apenergy.2020.115432.

[34] J. Yan, B.W. Yang, C.Y. Zhao, Investigation of hydration/dehydration processes in a fluidized bed reactor using $MgO/Mg(OH)_2$ thermochemical energy storage system, Sol. Energy 233 (2022) 630–645, https://doi.org/10.1016/j.solener.2021.12.013.

[35] J. Szekely, J.W. Evans, H.Y. Sohn, Reactions of porous solids, in: J. Szekely, J. W. Evans, H.Y. Sohn (Eds.), Gas-solid Reactions, Elsevier, 1976, pp. 108–175.

[36] A. Khawam, D.R. Flanagan, Solid-state kinetic models: basics and mathematical fundamentals, J. Phys. Chem. B 110 (35) (2006) 17315–17328, https://doi.org/10.1021/jp062746a.

[37] M. Pijolat, L. Favergeon, Chapter 5 – kinetics and mechanisms of solid-gas reactions, in: Handbook of Thermal Analysis and Calorimetry 6, 2018, pp. 173–212, https://doi.org/10.1016/B978-0-444-64062-8.00011-5.

[38] R.-J. Clark, M. Farid, Hydration reaction kinetics of $SrCl_2$ and $SrCl_2$-cement composite material for thermochemical energy storage, Sol. Energy Mater. Sol. Cells 231 (2021), 111311, https://doi.org/10.1016/j.solmat.2021.111311.

[39] B.H. Gilding, R. Kersner, The characterization of reaction-convection-diffusion processes by travelling waves, J. Differ. Equ. 124 (1) (1996) 27–79, https://doi.org/10.1006/jdeq.1996.0002.

[40] G. Zhao, S. Ruan, Time periodic traveling wave solutions for periodic advection–reaction–diffusion systems, J. Differ. Equ. 257 (4) (2014) 1078–1147, https://doi.org/10.1016/j.jde.2014.05.001.

[41] T. Cosgun, M. Sari, Traveling wave solutions and stability behaviours under advection dominance for singularly perturbed advection-diffusion-reaction processes, Chaos, Solitons Fractals 138 (2020), 109881, https://doi.org/10.1016/j.chaos.2020.109881.

[42] T.K. Perkins, O.C. Johnston, A review of diffusion and dispersion in porous media, Soc. Pet. Eng. J. 3 (1) (1963) 70–84, https://doi.org/10.2118/480-PA.

[43] J.R. Rumble, CRC Handbook of Chemistry and Physics, 103rd edition, CRC Press/Taylor & Francis, Boca Raton, FL, 2022 (Internet Version).

[44] J.P.M.Q. Delgado, Longitudinal and transverse dispersion in porous media, Chem. Eng. Res. Des. 85 (9) (2007) 1245–1252, https://doi.org/10.1205/cherd07017.

[45] L.-C. Sögütoglu, F. Birkelbach, A. Werner, H. Fischer, H. Huinink, O. Adan, Hydration of salts as a two-step process: water adsorption and hydrate formation, Thermochim. Acta 695 (2021), 178819, https://doi.org/10.1016/j.tca.2020.178819.

[46] H.S. Folger, Elements of Chemical Reaction Engineering, 5th ed., Prentice Hall, 2016.

[47] F.A.L. Dullien, Porous Media: Fluid Transport and Pore Structure, 2nd ed., Academic Press, 1992 (ISBN 978-0-12-223651-8).

[48] A.B. Yu, J. Bridgwater, A. Burbidge, On the modelling of the packing of fine particles, Powder Technol. 92 (3) (1997) 185–194, https://doi.org/10.1016/S0032-5910(97)03219-1.

[49] https://materials.springer.com/.

[50] L.-C. Sögütoglu, M. Steiger, J. Houben, D. Biemans, H.R. Fischer, P.A.J. Donkers, H. P. Huinink, O.C.G. Adan, Understanding the hydration process of salts: the impact of a nucleation barrier, Crystal Growth Des. 19 (4) (2019) 2279–2288, https://doi.org/10.1021/acs.cgd.8b01908.

[51] N. Mazur, S. Salviati, H. Huinink, A. Fina, F. Carosio, H. Fischer, O. Adan, Impact of polymeric stabilisers on the reaction kinetics of $SrBr_2$, Sol. Energy Mater. Sol. Cells 238 (2022), 111648, https://doi.org/10.1016/j.solmat.2022.111648.

[52] M.A.R. Blijlevens, N. Mazur, W. Kooijman, H.R. Fischer, H.P. Huinink, H. Meekes, E. Vlieg, A study of the hydration and dehydration transitions of $SrCl_2$ hydrates for use in heat storage, Sol. Energy Mater. Sol. Cells 242 (2022), 111770, https://doi.org/10.1016/j.solmat.2022.111770.

[53] R.W. Carling, Dissociation pressures and enthalpies of reaction in MgCI2·nH2O and CaCl2·NH3, J. Chem. Thermodyn. 13 (1982) 503–512, https://doi.org/10.1016/0021-9614(81)90105-1.